Sensors & Actuators: B. Chemical 378 (2023) 133152

Contents lists available at ScienceDirect

Sensors and Actuators: B. Chemical

journal homepage: www.elsevier.com/locate/snb

Ru(dcbpy)$_3^{2+}$-functionalized γ-cyclodextrin metal-organic frameworks as efficient electrochemiluminescence tags for the detection of CYFRA21-1 in human serum

Xiaofei Li [a], Xiang Ren [a], Lei Yang [a,*], Wei Wang [c], Dawei Fan [a], Xuan Kuang [a], Xu Sun [a], Qin Wei [a,d,**], Huangxian Ju [a,b]

[a] Key Laboratory of Interfacial Reaction & Sensing Analysis in Universities of Shandong, School of Chemistry and Chemical Engineering, University of Jinan, Jinan 250022, China
[b] State Key Laboratory of Analytical Chemistry for Life Science, School of Chemistry and Chemical Engineering, Nanjing University, Nanjing 210023, China
[c] Logistics Management Center of Yantai Customs District, Yantai 264000, China
[d] Department of Chemistry, Sungkyunkwan University, Suwon 16419, Republic of Korea

ARTICLE INFO

Keywords:
Electrochemiluminescence
Immunosensor
CYFRA21–1
Cyclodextrin
Metal organic frameworks

ABSTRACT

Electrochemiluminescence (ECL)-functionalized metal-organic frameworks (MOFs) have become one of the most favored topics in biomarker immunoassays. Herein, a biocompatible tris(4,4′-dicarboxylic acid-2,2′-bipyridyl) ruthenium(II) [Ru(dcbpy)$_3^{2+}$] functionalized γ-cyclodextrin MOF was freshly prepared as an ECL tag for analyzing cytokeratin 19 fragment 21–1 (CYFRA21–1), a quintessential biomarker of non-small cell lung cancer. As a green ECL carrier, γ-CD-MOF possessed a large cavity that can absorb enormous Ru(dcbpy)$_3^{2+}$ molecules, obtaining consecutive stable ECL signals using *N,N*-dibutyl-2-hydroxyethylamine (DBAE) as a coreactant. Further functionalization of palladium nanoparticles with Ru@ γ-CD-MOF not only facilitated the electron-transfer rate to boost the ECL emission but also immobilized the detection antibody (Ab_2) via a Pd-N bond. To fabricate the sensing substrate, a porous NH_2-MIL-125 (Ti) MOF was coated on the electrode to provide many binding sites for the capture antibody (Ab_1). Through the traditional sandwich-type sensing format, the assembled immunosensor manifested a linear range with a limit of detection of 0.048 pg/mL ($S/N = 3$) within a concentration gradient of 0.0001–50 ng/mL for CYFRA21–1 detection. Given this strategy's merits of favorable specificity, reliable accuracy and remarkable stability, this study highlighted the feasibility of fabricating γ-CD-based ECL tags for immunosensor construction, revealing this strategy's promising aptitude for bioanalysis and the clinical diagnosis of biomarkers.

1. Introduction

Lung cancer, as a fatal disease, has attracted much more concern due to its intensified incidence and death rate [1]. More than half of lung cancer cases are caused by non-small cell lung cancer (NSCLC) [2]. Tumor markers are proteins or other substances that cancer cells produce in larger quantities than normal cells. Various tumor markers have been identified and are in the clinical stage for diagnosis and treatment due to their extraordinary specificity and sensitivity [3]. Each kind of tumor marker is associated with at least one cancer type. Thus, early detection of tumor makers plays a significant role in lung cancer treatment to prevent the condition from deteriorating. Cytokeratin 19 fragment 21–1 (CYFRA21–1) has been considered an accurate biochemical indicator used for lung cancer clinical diagnosis at an early stage [4]. As an acid polypeptide, the specific expression of CYFRA21–1 in epithelial cells facilitates NSCLC assays [5]. To date, conventional methods for the detection of CYFRA21–1 have been exploited, including fluorometry [6], surface plasmon resonance analysis [7], immunoradiometric assay methods [8], immunocytochemistry [9], western blotting [10], flow cytometry (FCM) [11] and northern blotting polymerase chain reaction (PCR) [12]. Moreover, immunosensor technology is also an influential method we regularly use, such as

* Corresponding author.
** Corresponding author at: Key Laboratory of Interfacial Reaction & Sensing Analysis in Universities of Shandong, School of Chemistry and Chemical Engineering, University of Jinan, Jinan 250022, China.
E-mail addresses: yanglei_19940831@163.com (L. Yang), sdjndxwq@163.com (Q. Wei).

https://doi.org/10.1016/j.snb.2022.133152
Received 25 August 2022; Received in revised form 8 December 2022; Accepted 8 December 2022
Available online 13 December 2022

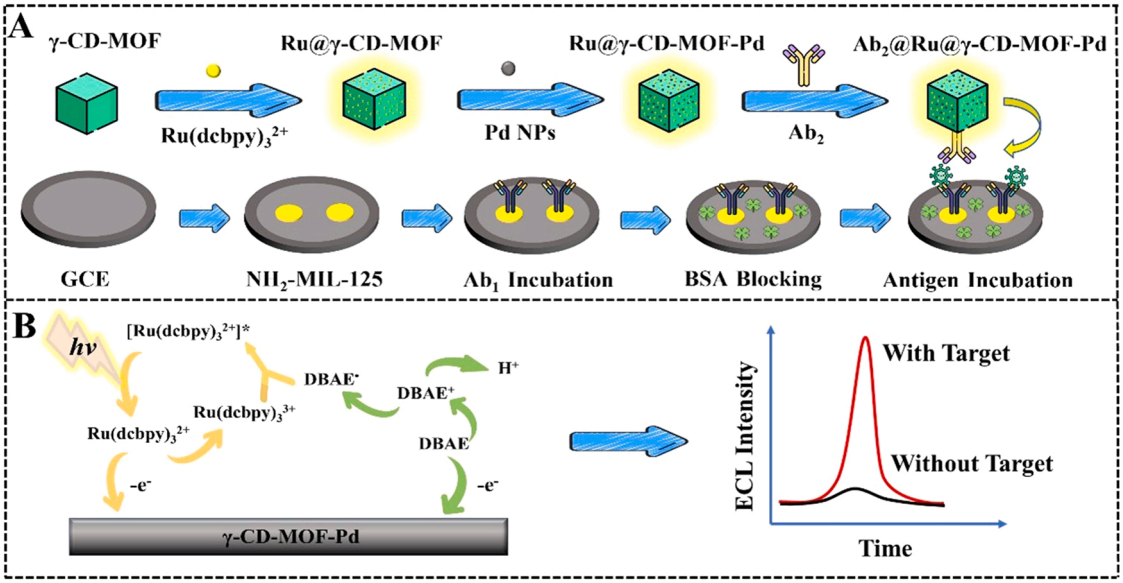

Scheme 1. The illustrated fabrication diagram (A) and sensing mechanism (B) of the ECL immunosensor.

photoelectrochemical immunosensors [13], electrochemical immunosensors [14], fluorescence immunosensors [15] and voltammetric immunosensors [16]. However, establishing a befitting analytical method to upgrade the sensitivity, biocompatibility and stability of CYFRA 21–1 remains a crucial task.

To date, electrochemiluminescence (ECL) stands out due to its sensitive detection, fast response, simple operation and wide linear range [17], which has been used for metal ion sensing [18], small molecule sensing [19], protein sensing [20], genosensing [21], and cell, bacterial, and virus sensing [21–23]. $Ru(bpy)_3^{2+}$ and its derivatives can be divided into ECL-active inorganic systems with many outstanding merits, including their high ECL efficiency and solubility in water and a variety of nonaqueous solvents [24]. However, efficient ECL was restrained in the absence of coreactant, but in the presence of coreactant, the ECL efficiency will be significantly increased [25] because a coreactant participates in chemical reactions and the excited states were generated by the reactions of intermediates that generated from the reaction of coreactants with luminophores [26]. Amine compounds such as polyethylenimine (PEI), tri-n-propylamine (TPrA), histidine, (2-dibutylamino)ethanol (DBAE) [27–31], etc.

However, the loading amount of Ru molecules directly influences the luminescence intensity of sensors [32]. Conventional materials for the loading of $Ru(bpy)_3^{2+}$-based materials are used, such as carbon nanotubes [33], g-C_3N_4 nanosheets (g-C_3N_4 NSs) [34], graphene [35], mesoporous silica nanoparticles (MSNs) [36], and Au nanoparticles (AuNPs) [37]. Thus, it is crucial to find a fitting substrate material for the loading of Ru molecules. Metal–organic frameworks (MOFs) possess merits of large surface areas, tunable pores and easy conjugation with biomolecules [38]. These merits endow MOFs with applications in gas storage [39], separation [40], chemical sensing [41] and molecular magnetism [42]. Furthermore, many luminescent guest species can be encapsulated in porous MOFs, endowing MOF materials with ECL activity and application prospects [43]. Based on the merits above, we properly introduced γ-cyclodextrin into a MOF to synthesize γ-CD-MOF by using potassium ions [44]. Compared with α- and β-CDs, γ-CD possesses -OCCO- binding groups on its primary and secondary faces [45], which allows γ-CD to be used for a wider range of applications in the preparation of nontoxic MOFs. The synthesized γ-CD-MOF exhibits favorable properties, such as superb biocompatibility, edibility, facile synthesis and easy modification [46].

Moreover, various functional groups on its surface allow MOFs to be labeled with a variety of molecules, including luminophores [47] and antibodies [48]. Noble metals play a prominent role in sensing analysis due to their special optical effects [49], catalytic capability [50] and biocompatibility [27]. Palladium nanoparticles (Pd NPs) stand out due to their excellent biocompatibility and superior electrocatalytic properties [51]. Simultaneously, the introduction of Pd NPs could significantly enhance the electronic transfer, improve the conductivity of the sensor and provide Pd-N bonds to capture many antibodies [52].

Herein, we utilized Pd NP-functionalized Ru@ γ-CD-MOF to form a versatile ECL immunosensor system for CYFRA21–1 detection. The γ-CD-MOF nanocrystals possessed high biocompatibility and remarkable adsorption capability because their cavities were utilized to stabilize volatile $Ru(dcbpy)_3^{2+}$ molecules and capture Pd NPs. The secondary antibody (Ab_2) was coupled with Pd NPs through Pd-N bonds, and Pd NPs further facilitated the electron transfer of Ru@ γ-CD-MOF. Then, the capture antibodies (Ab_1) were captured on an NH_2-MIL-125-decorated glassy carbon electrode (GCE) to construct the ECL immunosensing platform. By the merits of the ascendancy of Ru@ γ-CD-MOF-Pd and NH_2-MIL-125, the interfacial electron-transfer rate was greatly enhanced, which further heightened the ECL efficiency. With the optimization of the sensor, the assembled ECL sensor exhibited a wide linear range and low detection limit in CYFRA21–1 detection, implying its great potential in ultrasensitive ECL bioanalysis.

2. Experimental section

2.1. Synthesizing NH_2-MIL-125

With reference to a previous method [53], 2.905 g 2-aminoter-ephtalic acid and 1 mL of $TiCl_4$ were distributed in a mixture consisting of 40 mL of DMF and MeOH (with a ratio of 1:1) and stirred for 20 min until completely dissolved. Then, the mixture was transferred into a Teflon-lined autoclave and reacted at 120 °C for 72 h. After cooling, the solid products were washed with MeOH and DMF 3 times and collected by centrifugation (8000 rpm, 8 min). Finally, the acquired NH2-MIL-125 was dried overnight and stored at room temperature for further use.

2.2. Synthesizing NH_2-MIL-125 @Ab_1

Initially, 5 mg of NH_2-MIL-125 powder, Ab_1 (500 μL, 10 μg/mL), 100 μL of N-hydroxysuccinimide (NHS, 5 mmol) and 100 μL of 1-ethyl-3-(3-dimethylaminopropyl) carbodiimide (EDC, 10 mmol) were mixed and oscillated at 4 °C overnight. After rediffused in phosphate buffer solution

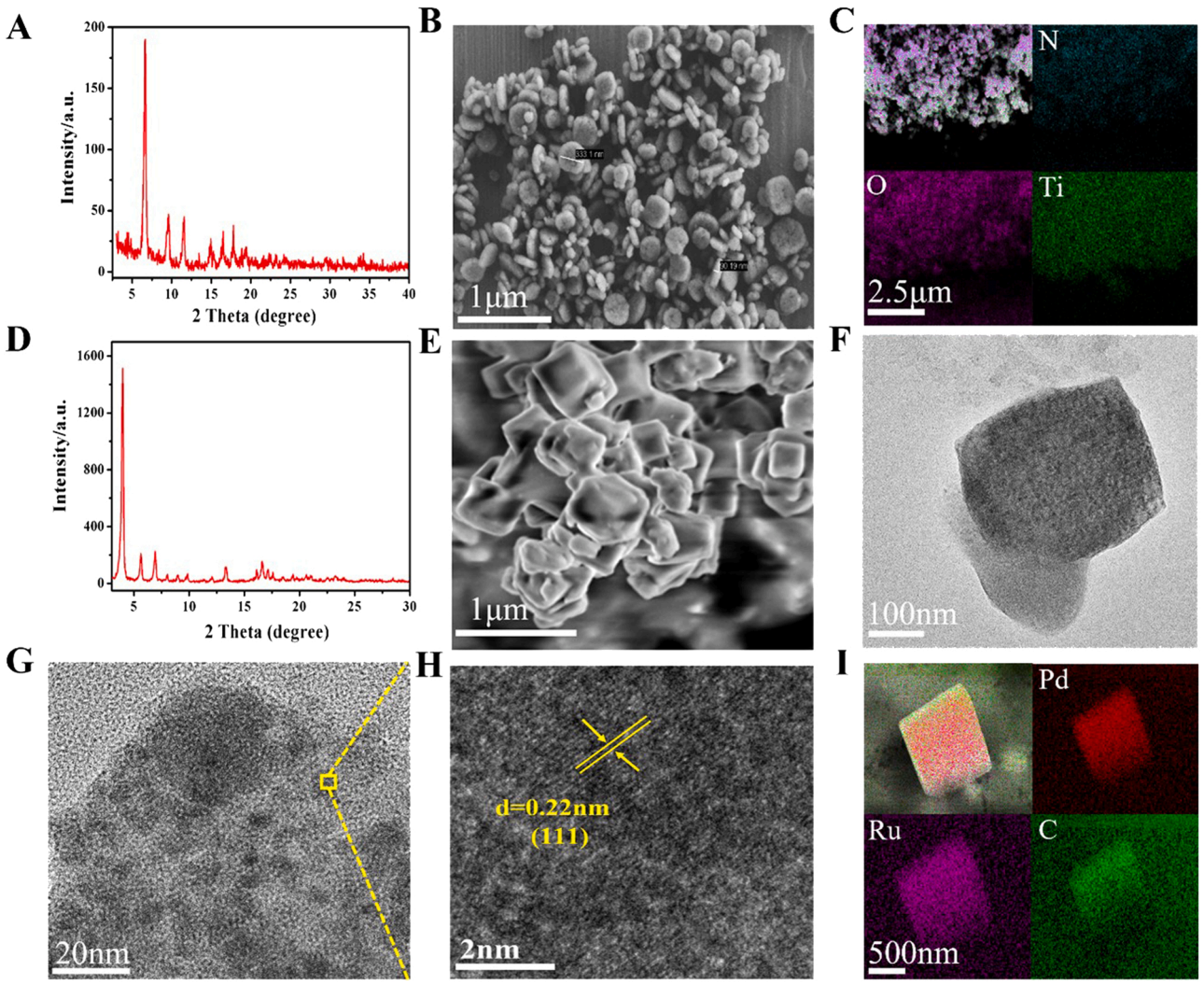

Fig. 1. (A) XRD pattern; (B) SEM image and (C) elemental mapping of NH_2-MIL-125(Ti); (D) XRD pattern, (E) SEM images of γ-CD-MOF; (F) TEM image of γ-CD-MOF-Pd (G) and the dispersion of Pd NPs; HRTEM image of Pd NPs (H); Elemental mapping of Ru@ γ-CD-MOF-Pd composites (I).

(PBS, pH 7.4), the finally obtained NH_2-MIL-125 @Ab_1 solution was placed in a 4 °C refrigerator before the next step.

2.3. Preparation of γ-CD-MOF

According to a previous method with delicate refinement [54], 30 mL of ultrapure water was used to disperse γ-CD (0.810 g) and KOH (0.280 g) to form a uniform mixture. After filtering the mixture with a syringe filter (0.45 μm), methanol vapor was then diffused into the mixture at 40 °C. When sedimentation was observed, the solution was centrifuged, and the supernatant was collected for a second crystallization. Next, 200 mg of CTAB and 30 mL of methanol were added and incubated overnight at room temperature. The emerged crystals were gathered by centrifugation at 8000 rpm, and the product was rinsed with i-PrOH 3 times. After that, dichloromethane was used to remove vestigial moisture for 72 h, and the final product was dried at 38 ℃ overnight.

2.4. Synthesizing Ru@ γ-CD-MOF-Pd

Trisodium citrate dehydrate (400 mM, 500 μL), Na_2PdCl_4 (32.5 mM, 60 μL), 50 mg γ-CD-MOF and 10 mg of PVP were sequentially added into ultrapure water (10 mL) and stirred for 10 min. At the same time, NaBH4 (200 mM, 20 μL) was dropped slowly into the above solution under stirring, and immediate darkening of the solution was observed. After 8 h of stirring, the formed γ-CD-MOF-Pd was centrifuged and dried overnight. Afterward, 5 mg of γ-CD-MOF-Pd and 500 μL of $Ru(dcbpy)_3^{2+}$ (0.5 mmol/L) were mixed and shaken for 12 h, and the obtained solution was stored at 4 °C before constructing the immunosensor.

2.5. Synthesizing the Ab_2 @Ru@ γ-CD-MOF-Pd

First, 500 μL of EDC/NHS solution with a concentration ratio of 1:5 was added into the mixture containing 2 mL Ru@ γ-CD-MOF-Pd solution (5 mg/mL) and Ab_2 (100 μL, 10 μg/mL). After shaking for 24 h at 4 °C, the Ab_2 @Ru@ γ-CD-MOF-Pd bioconjugates were formed in 1 mL of PBS (pH 7.4).

2.6. Fabrication of immunosensor

Scheme 1 showed the assembly process of the sensor. First, the glassy carbon electrode (GCE, Φ = 4 mm) was preprocessed to a mirror-like surface along with sequential rinsing with deionized water and ethanol and then dried in N_2 flow. Then, 6 μL of 5 mg/mL NH_2-MIL-125 @Ab_1 solution was sprinkled onto the electrodes and incubated at 4 °C. After 1 h, the GCE/NH_2-MIL-125 @Ab_1 substrate was successfully formed. Following modification with 3 μL of BSA (wt 1%), the nonspecific binding sites on the electrode surface were hindered. After 1 h, the

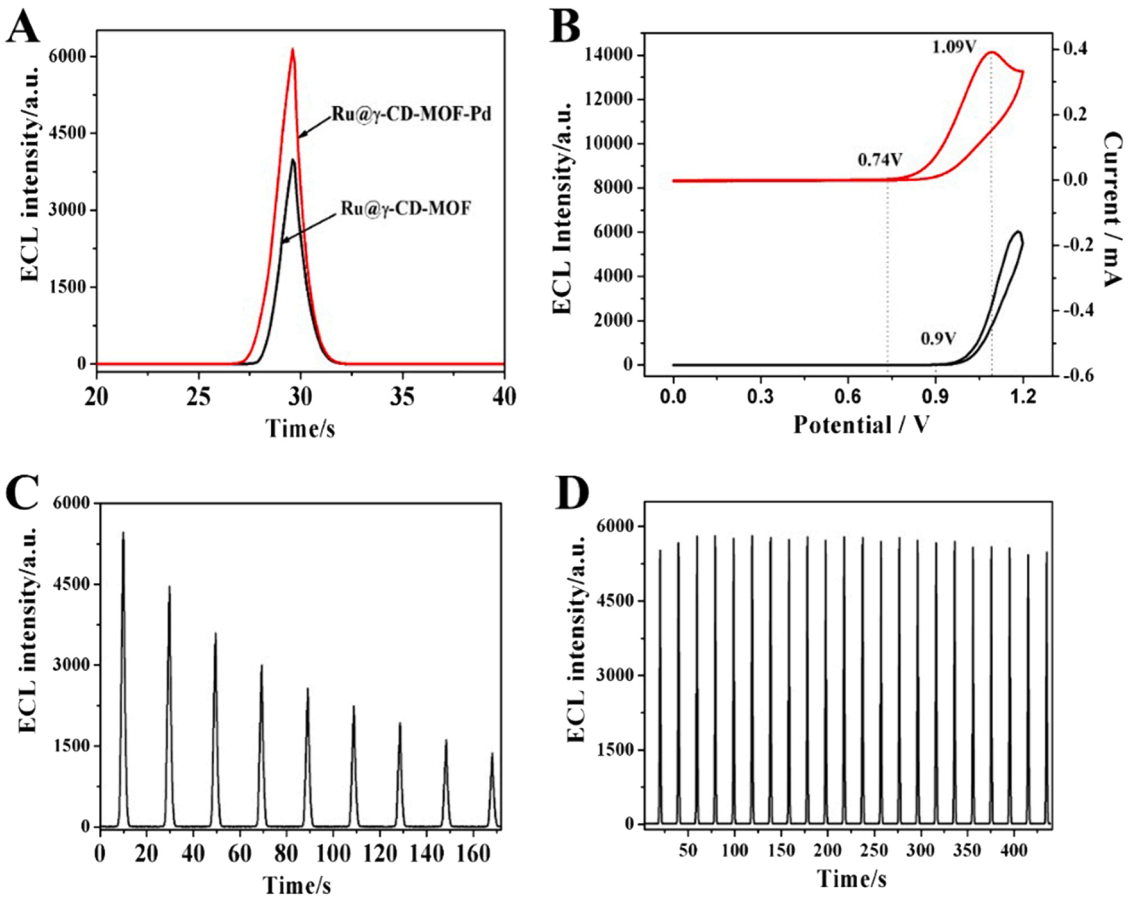

Fig. 2. ECL-time curves (A) of Ru@ γ-CD-MOF-Pd and Ru@ γ-CD-MOF; (B) ECL-potential curve (black curve) and CV curve (red curve) of the immunosensor. ECL intensity-time curves of $Ru(dcbpy)_3^{2+}$ (C) and Ru@ γ-CD-MOF-Pd (D).

excess BSA on the GCE/NH_2-MIL-125 @Ab_1/BSA surface was washed with PBS (pH 7.4). Next, 6 μL of CYFRA 21–1 antigen solution with a certain concentration was incubated on the GCE/NH_2-MIL-125 @Ab_1/BSA electrode for 2 h to form the GCE/NH_2-MIL-125 @Ab_1/BSA/CYFRA 21–1 electrode at 37 °C. Finally, 6 μL of Ab_2 @Ru@ γ-CD-MOF-Pd solution was dripped on the above electrode at 37 ℃ for 2 h to finish the sensor assembly process.

2.7. ECL measurements

The three-electrode system was implemented in PBS buffer (10 mL, pH 7.4) containing 50 mmol/L DBAE. The anodic potential range was set from 0 to 1.2 V. The photomultiplier tube (PMT) voltage was applied at 800 V with a scan rate of 100 mV/s. All ECL data were obtained via an ECL analyzer using cyclic voltammetry. Details of the materials, reagents and apparatus were further presented in the Supplementary Material.

3. Results and discussion

3.1. Characterization of different nanomaterials

The X-ray diffraction (XRD) pattern of NH_2-MIL-125(Ti) was investigated and shown in Fig. 1A. The diffraction peaks of NH_2-MIL-125(Ti) were in good accordance with the standard XRD pattern of NH_2-MIL-125 (Ti) [53], confirming the successful synthesis. The morphologies of NH_2-MIL-125 and γ-CD-MOF were characterized by scanning electron microscopy (SEM), as presented in Fig. 1B, from which it was viewed that the corn flake-like NH_2-MIL-125 had an average diameter of ~300 nm along with an average thickness of ~90 nm. Fourier transform infrared spectroscopy (FT-IR) was employed to confirm the amino groups of NH_2-MIL-125(Ti). As displayed in Fig. S1, an obvious absorption band at 3400 cm^{-1} could be attributed to the stretching vibration of the –NH_2 group, which indicated that the prepared NH_2-MIL-125 can immobilize Ab_1 via amide bonding. Further EDS analysis revealed uniformly distributed elements of N, O and Ti in NH_2-MIL-125(Ti), as shown in Fig. 1C.

The XRD pattern of γ-CD-MOF was investigated as well, and all the diffraction peaks in Fig. 1D were well matched with the known pattern of the γ-CD-MOF material[35]. Moreover, the morphology and size of γ-CD-MOF were investigated by SEM (Fig. 1E). The SEM image showed a block shape with a particle size of approximately 300–500 nm. EDS mapping (Fig. 1I) was applied to Ru@ γ-CD-MOF-Pd, and it could be seen that Ru, Pd, and C elements were uniformly distributed, indicating that Pd NPs were successfully combined with Ru@ γ-CD-MOF to form Ru@ γ-CD-MOF-Pd nanomaterials. To further support the above results, TEM and HRTEM were utilized to characterize the formed Pd NPs. The TEM image in Fig. 1G showed that multitudinous Pd NPs were scattered on the surface of porous cubes, and the HRTEM in Fig. 1H showed that Pd NPs had an average size of ~ 6 nm with a 0.22 nm lattice spacing, which was compatible with the reported value.

Additionally, the specific surface area, pore size distribution and average pore size of the specimens were evaluated by N_2 adsorption-desorption, and the results were shown in Fig. S2 and Table S1. The isotherms of γ-CD-MOF crystals and NH_2-MIL-125 both exhibited a type I shape, suggesting the existence of micropores. The calculated BET surface area showed that γ-CD-MOF was 804 m^2 g^{-1} with a pore size of approximately 2.2 nm. The Barrett—Joyner—Halenda analysis suggested that micropores accounted for the majority with diameters of ~0.6, 0.7, 0.9, and 1.7 nm, which was in accordance with a previous

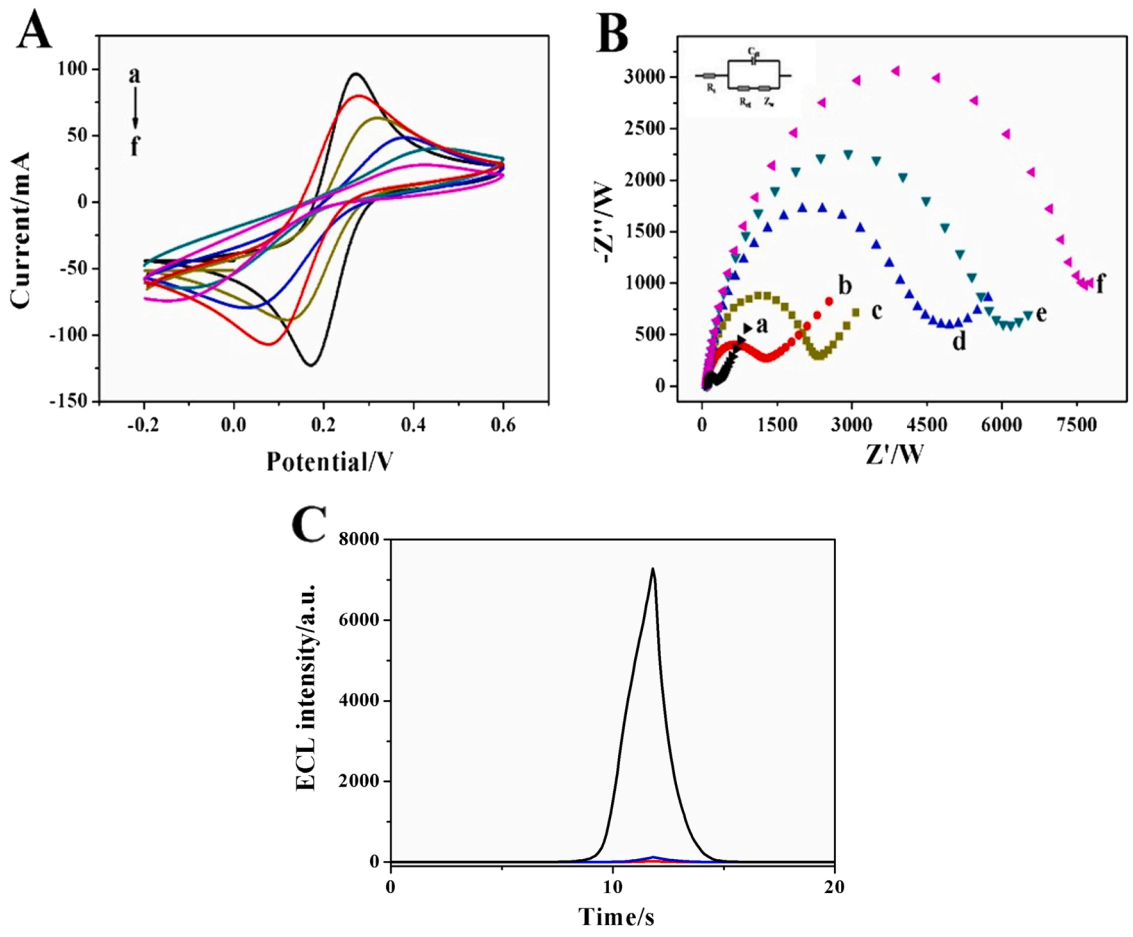

Fig. 3. CV curves (A) and EIS responses (B) for (a) bare GCE, (b) GCE/NH_2-MIL-125; (c) GCE/NH_2-MIL-125/Ab_1; (d) GCE/NH_2-MIL-125/Ab_1/BSA; (e) GCE/NH_2-MIL-125/Ab_1/BSA/CYFRA21–1; (f) GCE/NH_2-MIL-125/Ab_1/BSA/CYFRA21–1/Ab_2 @ γ-CD-MOF-Pd@Ru; (C) ECL-time curves of GCE/NH_2-MIL-125/Ab_1 (red curve), GCE/NH_2-MIL-125/Ab_1/BSA/CYFRA21–1 (blue curve), GCE/NH_2-MIL-125/Ab_1/BSA/CYFRA21–1/Ab_2 @ γ-CD-MOF-Pd@Ru (black curve).

report [54]. The NH_2-MIL-125 had a BET surface area of 4.7 $m^2\,g^{-1}$ with a pore size of approximately 5.9 nm. The occurrence of the mesoporous structure was positively confirmed by the Barrett—Joyner—Halenda method.

Moreover, an inductively coupled plasma optical emission spectrometer (ICP—OES) was used to determine the encapsulation ratio of $Ru(dcbpy)_3^{2+}$ in the prepared Ru@ γ-CD-MOF-Pd solution. According to the ICP—OES calibration curve, the linear relationship was presented as $y = 14426 \times c + 4841.7$. As shown in Table S2, the obtained results showed that the encapsulated $Ru(dcbpy)_3^{2+}$ was 0.163 μmol, and the encapsulation ratio was calculated to be approximately 65.28%.

3.2. Possible mechanism of the ECL biosensor

The efficient signal enhancement by Pd NPs was proved by the obvious difference between the red curve and the black curve in Fig. 2A. Compared with unmodified Pd NPs, the Ru@ γ-CD-MOF-Pd performed a much stronger ECL intensity, which could be attributed to the good electrocatalytic activity of Pd NPs toward the ECL reaction, implying that Pd NPs acted as coreaction accelerators for signal amplification. As shown in Fig. 2D, obvious constant peaks of Ru@ γ-CD-MOF were obtained compared with pure $Ru(dcbpy)_3^{2+}$ (Fig. 2C), which implied that the cubic porous structure of γ-CD could efficiently stabilize $Ru(dcbpy)_3^{2+}$ molecules to achieve stable ECL signals for immunosensing applications.

Benefiting from these merits, the feasible ECL mechanism of this sensor could be adumbrated as shown below (Eqs. 1–4). As displayed in Fig. 2B, an obvious oxidative process originated along with the injection of the coreactant DBAE, whose onset potential occurred at 0.74 V and the oxidation peak potential at 1.09 V, in which process DBAE was oxidized to $DBAE^+$ and then quickly deprotonated to form a large amount of reductive $DBAE^{\bullet}$ radicals along with catalytic promotion by Pd NPs (Eq. 1). At the same time, $Ru(dcbpy)_3^{2+}$ was oxidized to form oxidative $Ru(dcbpy)_3^{3+}$ (Eq. 2). By that time, the ECL emission process was triggered from 0.90 V and then reached a maximum at 1.20 V. In this process, those $DBAE^{\bullet}$ radicals react with those oxidative $Ru(dcbpy)_3^{3+}$ to generate the excited $[Ru(dcbpy)_3^{2+}]^*$ (Eq. 3). After relaxing to the ground state, light was emitted (Eq. 4).

$$DBAE - e^- \rightarrow DBAE^+ \xrightarrow{\text{Pd NPs}} H^+ + DBAE^{\bullet}(\text{more}) \quad (1)$$

$$Ru(dcbpy)3^{2+} - e^- \rightarrow Ru(dcbpy)3^{3+} \quad (2)$$

$$DBAE^{\bullet} + Ru(dcbpy)3^{3+} \rightarrow [Ru(dcbpy)3^{2+}]^* \quad (3)$$

$$[Ru(dcbpy)3^{2+}]^* \rightarrow Ru(dcbpy)3^{2+} + h\nu \quad (4)$$

3.3. Characterization of the Proposed ECL Immunosensor

Cyclic voltammetry (CV) was shown in Fig. 3A to elucidate the successful fabrication of the immunosensor. A clear reversible redox peak of bare GCE was observed in 5 mmol/L $[Fe(CN)_6]^{3-/4-}$ solution (curve a). After modifying the material of NH_2-MIL-125, a conspicuously decreased peak current (curve b) was observed, which can be ascribed to its poor electrical conductivity. Meanwhile, with the immobilization of Ab_1, BSA and CYFRA 21–1 (curves c, d, and e), the oxidation and

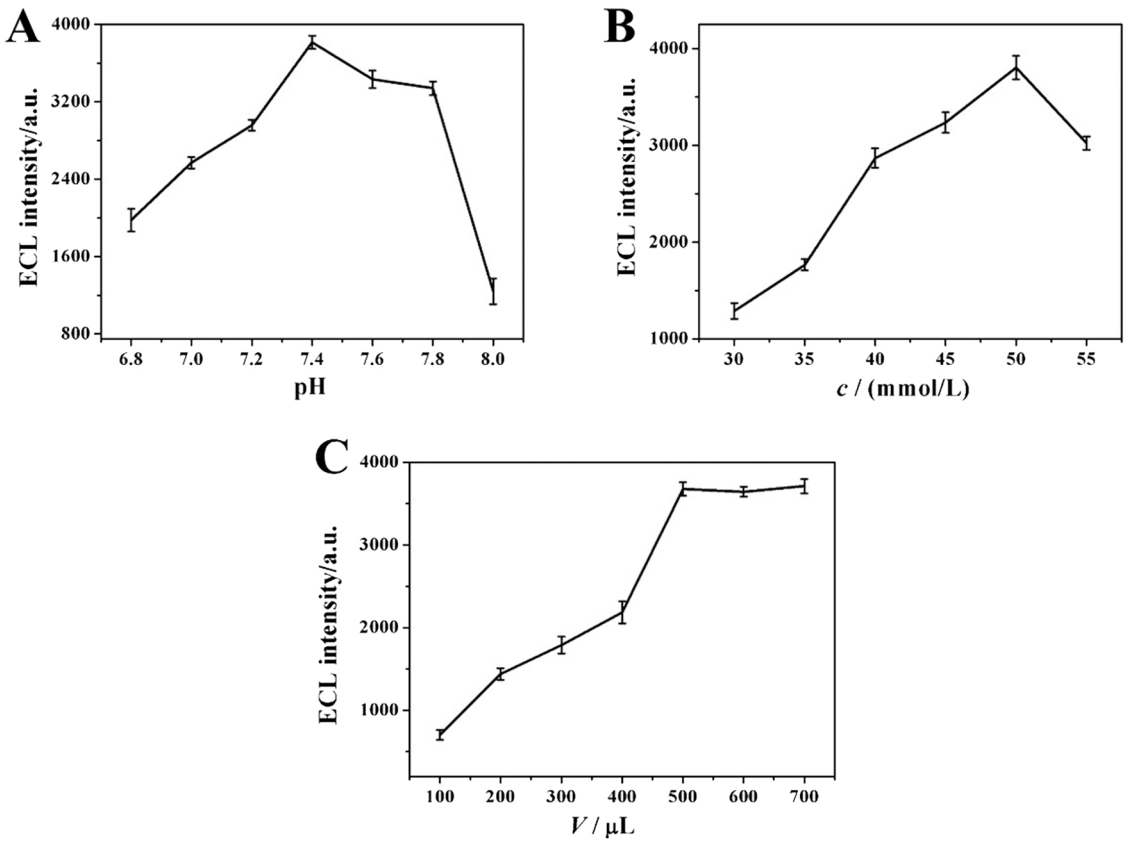

Fig. 4. Conditions: (A) pH value, (B) concentration of DBAE and (C) volume of $Ru(dcbpy)_3^{2+}$. (Error bars: SD, n = 5).

reduction peak currents decreased sequentially due to the non-conductivity of the proteins for electron transfer. With the final modification of Ru@ γ-CD-MOF-Pd@Ab_2, the redox current intensity in curve f further decreased, proving its successful conjugation with CYFRA21–1.

Furthermore, electrochemical impedance spectroscopy (EIS) was further conducted to confirm the successful construction of the immunosensor. As shown in Fig. 3B, the electron transfer resistance (R_{et}) of NH_2-MIL-125 (curve b) was increased relative to that of bare GCE (curve a) due to the poor electrical conductivity of the NH_2-MIL-125 material. When the electrode was coated with Ab_1, BSA, and CYFRA21–1 (curves c, d and e), the impedance was further expanded, suggesting the successful modification of biosubstances on GCE. Moreover, with the Ab_2 bioconjugate (cure f) coated on the electrode, the impedance value further increased. Both CV and EIS characterization were identical, which confirmed the successful construction of the immunosensor.

To confirm the successful immobilization of $Ru(dcbpy)_3^{2+}$ on γ-CD-MOF and the fabrication of the ECL sensor, corresponding ECL intensity-time curves were collected in PBS (10 mL, pH 7.4) containing 50 mmol/L DBAE. As shown in Fig. 3C, when the electrodes were separately coated with NH_2-MIL-125/Ab_1 (red curve) and NH_2-MIL-125/Ab_1/BSA/CYFRA21–1 (50 ng/mL) was decorated (blue curve), almost no ECL signals were detected in the same PBS electrolytes. However, robust ECL responses was promisingly detected when Ab_2 @Ru@ γ-CD-MOF-Pd was further attached to the electrode surface (black curve), suggesting the crucial role of Ab_2 @Ru@ γ-CD-MOF-Pd of being an efficient signal-indicator in the proposed immunosensor.

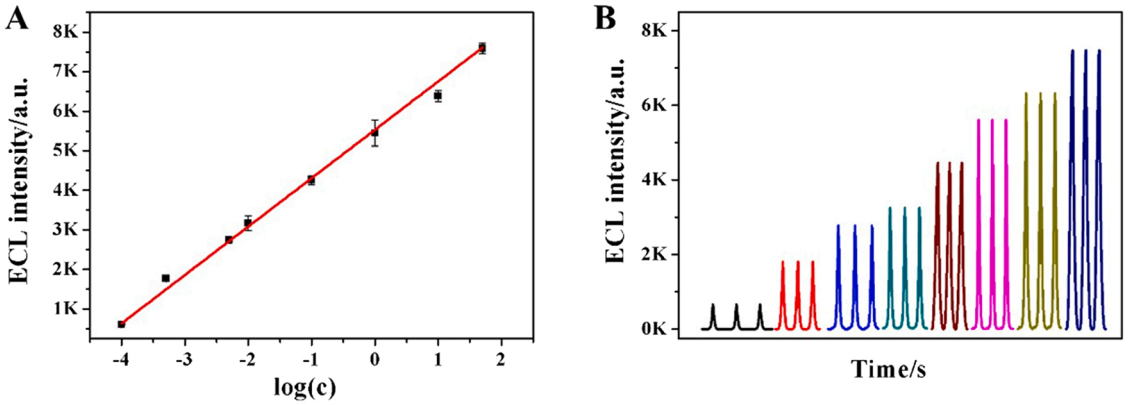

Fig. 5. Calibration curve (A) and (B) the concentrations of CYFRA21–1 from 0.1 pg/mL to 50 ng/mL. The conditions were performed in PBS (10 mL, pH 7.4) containing 50 mmol/L DBAE. (Error bars: SD, n = 5).

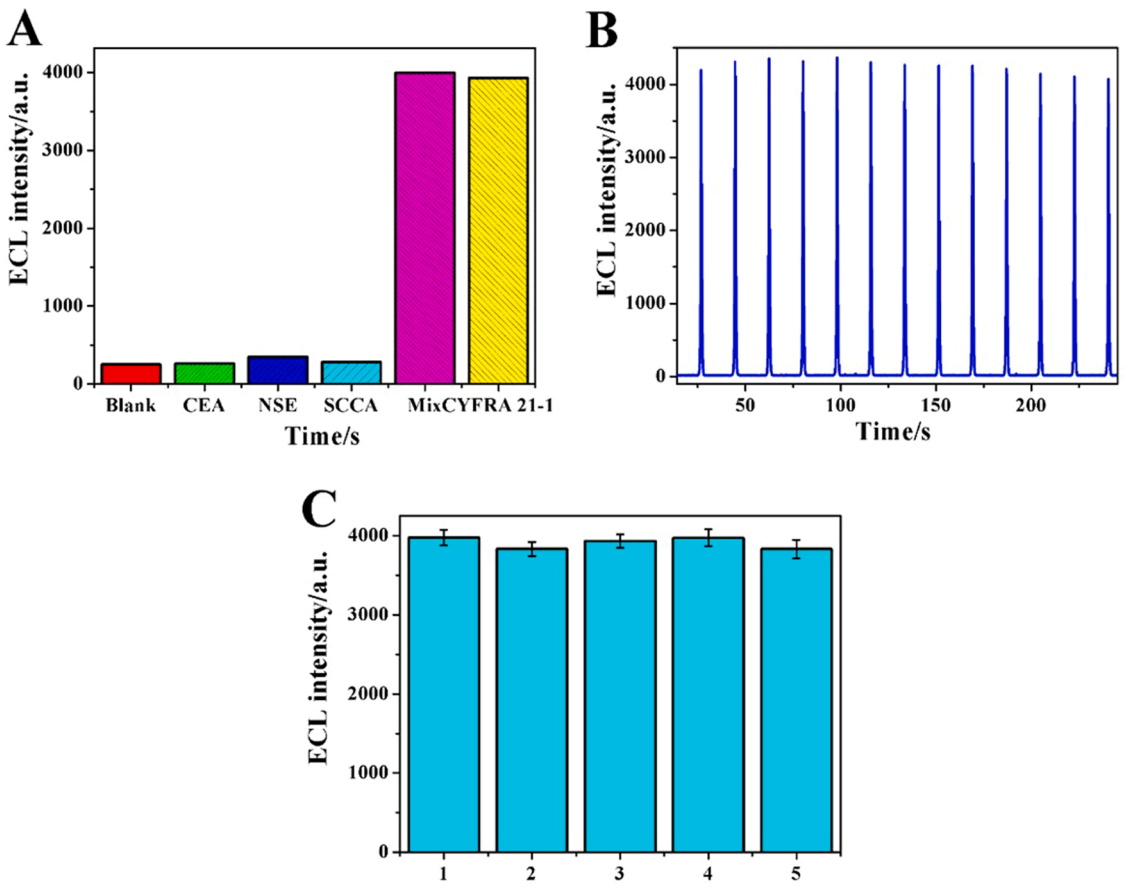

Fig. 6. (A) ECL intensity of the sensor with various interferences: blank, 10 ng/mL CEA, NSE, SCCA, CYFRA21–1, and a mixture (containing 10 ng/mL CEA, NSE, SCCA and 0.1 ng/mL CYFRA21–1). (B) Consecutive operation stabilization of the ECL immunosensor for 13 cycles. (C) Repeatability of ECL immunosensors by five parallel measurements in the presence of 0.1 ng/mL CYFRA 21–1. (Error bars: SD, n = 5).

3.4. Condition optimization for the immunosensor

To investigate the optimal conditions for the sensor to achieve maximum performance, we optimized the condition of the immunosensor in the evaluation of the pH value of PBS, added volume of Ru(dcbpy)$_3^{2+}$ solution, and the concentration of DBAE. The Fig. 4A illustrated the relationship between the pH effect of PBS and the corresponding ECL signal. The ECL intensity reached the highest value when the pH value of the PBS was 7.4. From Fig. 4B, the maximum value occurred at 50 mmol/L, which was nominated as the optimum concentration of DBAE. Moreover, the added volume of Ru(dcbpy)$_3^{2+}$ was another key factor interfering with the construction of the immunosensor. As revealed in Fig. 4C, the ECL emission of the sensor increased with increasing volume of Ru(dcbpy)$_3^{2+}$ and reached a plateau at 500 μL. Therefore, the optimum volume was chosen to be 500 μL for the subsequent investigation.

3.5. ECL detection of CYFRA 21–1

Under optimized conditions, various concentrations of CYFRA21–1 were utilized to investigate the analytical performance of the designed immunosensor. As depicted in Fig. 5A and B, the ECL signal increased correspondingly with the level of CYFRA 21–1 from 0.1 pg/mL to 50 ng/mL. The linear equation was I = 1223.5 log c + 5529.9, and the correlation coefficient was 0.99 along with a low detection limit of 0.048 pg/mL ($S/N = 3$). Additionally, compared with other detection approaches for CYFRA21–1 in Table S3, our developed ECL immunosensor exhibited a lower detection limit and a wider calibration range. This might be attributed to the superior ECL properties of Ru(dcbpy)$_3^{2+}$ and the nontoxic biocompatibility of γ-CD-MOF. By combining the advantages of Ru(dcbpy)$_3^{2+}$ and γ-CD-MOF, the ECL efficiency was greatly improved, and a stable ECL response was obtained. It could be concluded that the proposed ECL immunosensor had a superior performance for CYFRA21–1 measurements.

3.6. Selectivity, stability, and repeatability of the immunosensor

To investigate the selectivity of the ECL sensor for CYFRA21–1 analysis, the study was conducted by using different nontarget substances, such as neuron-specific enolase (NSE), carcinoembryonic antigen (CEA) and squamous cell carcinoma antigen (SCCA). As illustrated in Fig. 6 A, nontarget substances, including CEA, NSE and SCCA, exhibited quite low and near ECL intensities at a 100-fold concentration (10 ng/mL). Nonetheless, all the mixture samples had similar ECL intensities compared with pure CYFRA21–1 (0.1 ng/mL), and the relative standard deviation (RSD) values were 1.2%. In addition, the stability was determined under 0.1 ng/mL CYFRA21–1 by consecutive CV scanning for 13 cycles with an RSD value of 2.2% (Fig. 6B). Moreover, the repeatability of the proposed immunosensors was presented in Fig. 6 C. Five electrodes with their own ECL intensities showed a low RSD of 1.8%, demonstrating the superior reproducibility of the fabricated immunosensor.

3.7. Application of the ECL immunoassay method

We evaluated the possibility of the assembled ECL sensor for CYFRA21–1 detection in serum specimens with the standard addition method. The original concentration was properly diluted, and then

diverse concentrations of CYFRA21–1 were added to the above samples. As revealed in Table S4, the recovery rate was between 92.7% and 102.0%, and the RSD was between 1.1% and 3.2%, implying that the assembled ECL sensor had promising applications for CYFRA21–1 detection.

4. Conclusion

In this work, the feasibility of using $Ru(dcbpy)_3^{2+}$-encapsulated γ-CD-MOF as an ECL tag to develop a sensitive immunoassay for CYFRA21–1 detection was successfully demonstrated. The obtained Ru@ γ-CD-MOF composite possessed good biocompatibility and remarkable adsorption capability for stabilizing an enormous amount of $Ru(dcbpy)_3^{2+}$ molecules, achieving strong and stable ECL signals in the presence of DBAE as the coreactant. With the assistance of the electroactive NH_2-MIL-125 (Ti) MOFs as a qualified sensing substrate that can efficiently capture Ab_1 for target detection, the proposed ECL immunoassay exhibited promising analytical performance for CYFRA21–1 at an ultratrace level along with good specificity. This work indicated a practical pathway for designing biocompatible γ-CD-MOF-based ECL active tags for sensitive immunoassays of CYFRA21–1 and other lung cancer-related biomarkers.

CRediT authorship contribution statement

Xiaofei Li: Conceptualization, Data curation, Writing – original draft. **Xiang Ren:** Methodology, Data curation. **Lei Yang**: Methodology, Writing – review & editing. **Wei Wang**: Methodology, Writing – review & editing. **Dawei Fan:** Methodology, data curation. **Xuan Kuang:** Writing – review & editing. **Xu Sun:** Formal analysis. **Qin Wei**: Supervision, Funding acquisition, Project administration, **Huangxian Ju:** Funding acquisition, Formal analysis.

Appendix A. Supplementary data

Reagents and materials, Apparatus, FT-IR of NH_2-MIL-125(Ti), BET & BJH tests of NH_2-MIL-125(Ti) & γ-CD-MOF, ICP-OES analysis of Ru contents in Ru@ γ-CD-MOF-Pd, Comparison of CYFRA 21–1 Detection Using Other Methods with the Proposed ECL Immunosensors, Recovery Results of CYFRA 21–1 in Serum Samples.

Declaration of Competing Interest

The authors declare that they have no known competing financial interests or personal relationships that could have appeared to influence the work reported in this paper.

Data Availability

Data will be made available on request.

Acknowledgments

This study was supported by the National Natural Science Foundation of China (Nos. 22274062, 21890741), Jinan Scientific Research Leader Workshop Project (2019GXRC027), Special Foundation for Taishan Scholar Professorship of Shandong Province.

Appendix A. Supporting information

Supplementary data associated with this article can be found in the online version at doi:10.1016/j.snb.2022.133152.

References

[1] Y.W. Zhao, L. He, B.H. Huang, W.D. Zhang, A.I. Hu, B.L. Li, S.Q. Liao, N. Wang, Identification of a novel DNA aptamer that selectively targets lung cancer serum, RSC Adv. 11 (2021) 33759–33769.
[2] L. Xu, X. Huang, Y. Lou, W. Xie, H. Zhao, Regulation of apoptosis, autophagy and ferroptosis by non-coding RNAs in metastatic non-small cell lung cancer (Review), Exp. Ther. Med. 23 (2022) 352.
[3] B. Babamiri, R. Hallaj, A. Salimi, Ultrasensitive electrochemiluminescence immunoassay for simultaneous determination of CA125 and CA15-3 tumor markers based on PAMAM-sulfanilic acid-$Ru(bpy)_3^{2+}$ and nanocomposite, Biosens. Bioelectron. 99 (2018) 353–360.
[4] M.L. Yola, N. Atar, N. Özcan, A novel electrochemical lung cancer biomarker cytokeratin 19 fragment antigen 21-1 immunosensor based on Si_3N_4/MoS_2 incorporated MWCNTs and core–shell type magnetic nanoparticles, Nanoscale 13 (2021), 4660-4469.
[5] Y. Kagawa, K. Sone, T. Oguri, M. Horiuchi, S. Fukuda, T. Uemura, O. Takakuwa, K. Maeno, K. Fukumitsu, Y. Kanemitsu, T. Tajiri, H. Ohkubo, M. Takemura, Y. Ito, A. Niimi, Predictive role of CYFRA 21-1 for S-1 monotherapy in non-small cell lung cancer patients, Respir. Investig. 60 (2022) 393–399.
[6] T. Tsumuraya, T. Sato, M. Hirama, I. Fujii, Highly sensitive and practical fluorescent sandwich ELISA for ciguatoxins, Anal. Chem. 90 (2018) 7318–7324.
[7] D. Garoli, E. Calandrini, G. Giovannini, A. Hubarevich, V. Caligiuri, F. De, Angelis, Nanoporous gold metamaterials for high sensitivity plasmonic sensing, Nanoscale Horiz. 4 (2019) 1153–1157.
[8] H. Sakahara, T. Kousaka, H. Kobayashi, Z. Yao, M. Imamura, T. Mori, Serum cytokeratin-19 measured by cyfra21-1 assay in patients with gastrointestinal and gynecologic malignancy, Int. J. Oncol. 5 (1994) 1137–1140.
[9] Y.H. Zhu, C.C. Ren, L. Yang, X.A. Zhang, L. Liu, Z.X. Wang, Performance of p16/Ki67 immunostaining, HPV E6/E7 mRNA testing, and HPV DNA assay to detect high-grade cervical dysplasia in women with ASCUS, BMC Cancer 19 (2019) 271.
[10] X. Hun, B.R. Liu, Y. Meng, Ultrasensitive chemiluminescence assay for the lung cancer biomarker cytokeratin 21-1 via a dual amplification scheme based on the use of encoded gold nanoparticles and a toehold-mediated strand displacement reaction, Microchim. Acta 184 (2017) 3953–3959.
[11] W.J. Lan, Y.M. Lin, Z.H. Men, L. Yan, Surface-decorated S. cerevisiae for flow cytometric array immunoassay, Anal. Bioanal. Chem. 409 (2017) 5259–5267.
[12] A. Mishra, N. Singh, D.K. Sahu, S. Kumar, 33P Expression of biomarkers IDH1, CEA, TPA and CYFRA21-1 in peripheral blood and tissue of non-small cell lung carcinoma patients detected by real-time PCR, J. Thorac. Oncol. 13 (2018) S18.
[13] S.T. Zhang, C. Wang, T.T. Wu, D.W. Fan, L.H. Hu, H. Wang, Q. Wei, D. Wu, A sandwiched photoelectrochemical biosensing platform for detecting Cytokeratin-19 fragments based on Ag_2S-sensitized BiOI/Bi_2S_3 heterostructure amplified by sulfur and nitrogen co-doped carbon quantum dots, Biosens. Bioelectron. 196 (2022), 113703.
[14] K. Hu, J.M. Cheng, K.B. Wang, Y.Q. Zhao, Y.J. Liu, H.X. Yang, Z.Q. Zhang, Sensitive electrochemical immunosensor for CYFRA21-1 detection based on AuNPs@MoS_2@Ti_3C_2Tx composites, Talanta 238 (2022), 122987.
[15] L.J. Ao, T. Liao, L. Huang, S. Lin, K. Xu, J.T. Ma, S.R. Qiu, X.Y. Wang, Q.Q. Zhang, Sensitive and simultaneous detection of multi-index lung cancer biomarkers by an NIR-II fluorescence lateral-flow immunoassay platform, Chem. Eng. J. 436 (2022), 135204.
[16] L. Qu, L. Yang, Y.Y. Li, X. Ren, H. Wang, D.W. Fan, X.Y. Wang, Q. Wei, H.X. Ju, Dual-signaling electrochemical ratiometric method for competitive immunoassay of CYFRA21-1 based on urchin-like Fe_3O_4@PDA-Ag and $Ni_3Si_2O_5(OH)_4$-Au absorbed methylene blue nanotubes, ACS Appl. Mater. Interfaces 13 (2021) 5795–5802.
[17] J. Zhao, J.H. Luo, D. Liu, Y. He, Q. Li, S.H. Chen, R. Yuan, A coreactant-free electrochemiluminescence (ECL) biosensor based on in situ generating quencher for the ultrasensitive detection of microRNA, Sens. Actuators B-Chem. 316 (2020), 128139.
[18] J.M. Xu, Y. Zhang, L. Li, Q.K. Kong, L.N. Zhang, S.G. Ge, J.H. Yu, Colorimetric and electrochemiluminescence dual-mode sensing of lead ion based on integrated lab-on-paper device, ACS Appl. Mater. Interfaces 10 (2018) 3431–3440.
[19] W. Zhao, H.Y. Chen, J.J. Xu, Electrogenerated chemiluminescence detection of single entities, Chem. Sci. 12 (2021) 5720–5736.
[20] C. Han, W.W. Guo, Fluorescent noble metal nanoclusters loaded protein hydrogel exhibiting anti-biofouling and self-healing properties for electrochemiluminescence biosensing applications, Small 16 (2020) 2002621.
[21] B. Babamiri, D. Bahari, A. Salimi, Highly sensitive bioaffinity electrochemiluminescence sensors: recent advances and future directions, Biosens. Bioelectron. 142 (2019), 111530.
[22] C. Cui, Y. Chen, D.C. Jiang, H.Y. Chen, J.R. Zhang, J.J. Zhu, Steady-state electrochemiluminescence at single semiconductive titanium dioxide nanoparticles for local sensing of single cells, Anal. Chem. 91 (2019) 1121–1125.
[23] H. Ding, W.L. Guo, L.R. Ding, B. Su, Confined electrochemiluminescence at microtube electrode ensembles for local sensing of single cells†, Chin. J. Chem. 39 (2021) 2911–2916.
[24] X.J. Li, S.Q. Yu, T. Yan, Y. Zhang, B. Du, D. Wu, Q. Wei, A sensitive electrochemiluminescence immunosensor based on $Ru(bpy)_3^{2+}$ in 3D CuNi oxalate as luminophores and graphene oxide–polyethylenimine as released $Ru(bpy)_3^{2+}$ initiator, Biosens. Bioelectron. 89 (2017) 1020–1025.
[25] S.G. Sun, Y. Yang, F.Y. Liu, Y. Pang, J.L. Fan, L.C. Sun, X.J. Peng, Study of highly efficient bimetallic ruthenium tris-bipyridyl ECL labels for coreactant system, Anal. Chem. 81 (2009) 10227–10231.

[26] Y. Li, L. He, C.Z. Huang, Y.F. Li, Silver-based metal-organic gels as novel coreactant for enhancing electrochemiluminescence and its biosensing potential, Biosens. Bioelectron. 134 (2019) 29–35.
[27] D.N. Han, B. Goudeau, D.C. Jiang, D.J. Fang, N. Sojic, Electrochemiluminescence microscopy of cells: essential role of surface regeneration, Anal. Chem. 93 (2021) 1652–1657.
[28] Y. He, Y.Q. Chai, R. Yuan, H.J. Wang, L.J. Bai, Y.L. Cao, Y.L. Yuan, An ultrasensitive electrochemiluminescence immunoassay based on supersandwich DNA structure amplification with histidine as a co-reactant, Biosens. Bioelectron. 50 (2013) 294–299.
[29] H.J. Tang, W.X. Chen, D.D. Li, X.L. Duan, S.J. Ding, M. Zhao, J. Zhang, Luminol-based ternary electrochemiluminescence nanospheres as signal tags and target-triggered strand displacement reaction as signal amplification for highly sensitive detection of Helicobacter pylori DNA, Sens. Actuators B-Chem. 293 (2019) 304–311.
[30] E. Villani, G. Valenti, M. Marcaccio, L. Mattarozzi, S. Barison, D. Garoli, S. Cattarin, F. Paolucci, Coreactant electrochemiluminescence at nanoporous gold electrodes, Electrochim. Acta 277 (2018) 168–175.
[31] L.L. Xue, L.H. Guo, B. Qiu, Z.Y. Lin, G.N. Chen, Mechanism for inhibition of Ru $(bpy)_3^{2+}$/DBAE electrochemiluminescence system by dopamine, Electrochem. Commun. 11 (2009) 1579–1582.
[32] G.B. Hu, C.Y. Xiong, W.B. Liang, X.S. Zeng, H.L. Xu, Y. Yang, L.Y. Yao, R. Yuan, D. R. Xiao, Highly stable mesoporous luminescence-functionalized MOF with excellent electrochemiluminescence property for ultrasensitive immunosensor construction, ACS Appl. Mater. Interfaces 10 (2018) 15913–15919.
[33] L. Tian, X.R. Wang, K.X. Wu, Y. Hu, Y. Wang, J. Lu, Ultrasensitive electrochemiluminescence biosensor for dopamine based on ZnSe, graphene oxide@multi walled carbon nanotube and $Ru(bpy)_3^{2+}$, Sesn. Actuators B-Chem. 286 (2019) 266–271.
[34] Y.F. Wang, Y. Zhang, H.F. Sha, X. Xiong, N.Q. Jia, Design and biosensing of a ratiometric electrochemiluminescence resonance energy transfer aptasensor between a g-C_3N_4 nanosheet and Ru@MOF for amyloid-β protein, ACS Appl. Mater. Interfaces 11 (2019) 36299–36306.
[35] J.J. Zhang, W.J. Liu, W. Gong, N. Liu, Y.T. Jia, D. Ding, Z.W. Ning, Ultrasensitive determination of microcystin-leucine-arginine (MCLR) by an electrochemiluminescence (ECL) immunosensor with graphene nanosheets as a scaffold for cadmium-selenide quantum dots (QDs), Anal. Lett. 54 (2021) 2523–2536.
[36] Y. Chen, Z.G. Chen, L.S. Fang, A.B. Weng, F. Luo, L.G. Guo, B. Qiu, Z.Y. Lin, electrochemiluminescence sensor for cancer cell detection based on H_2O_2-triggered stimulus response system, J. Anal. Test. 4 (2020) 128–135.
[37] Y.J. Liu, H.D. Zhang, B.X. Li, J.W. Liu, D.C. Jiang, B.H. Liu, N. Sojic, Single biomolecule imaging by electrochemiluminescence, J. Am. Chem. Soc. 143 (2021) 17910–17914.
[38] Z.C. Jin, X.R. Zhu, N.G. Wang, Y.F. Li, H.X. Ju, J.P. Lei, Electroactive metal–organic frameworks as emitters for self-enhanced electrochemiluminescence in aqueous medium, Angew. Chem. Int. Ed. 59 (2020) 10446–10450.
[39] H. Daglar, H.C. Gulbalkan, G. Avci, G.O. Aksu, O.F. Altundal, C. Altintas, I. Erucar, S. Keskin, Effect of metal–organic framework (MOF) database selection on the assessment of gas storage and separation potentials of MOFs, Angew. Chem. Int. Ed. 60 (2021) 7828–7837.
[40] H. Xiang, Y. Shao, A. Ameen, H.H. Chen, W.T. Yang, P. Gorgojo, F.R. Siperstein, X. L. Fan, Q.H. Pan, Adsorptive separation of C_2H_6/C_2H_4 on metal-organic frameworks (MOFs) with pillared-layer structures, Sep. Purif. Technol. 242 (2020), 116819.
[41] J.F. Olorunyomi, S.T. Geh, R.A. Caruso, C.M. Doherty, Metal–organic frameworks for chemical sensing devices, Mater. Horiz. 8 (2021) 2387–2419.
[42] H.B. Meng, C. Zhao, M.Z. Nie, C.R. Wang, T.S. Wang, Optically controlled molecular metallofullerene magnetism via an azobenzene-functionalized metal–organic framework, ACS Appl. Mater. Interfaces 10 (2018) 32607–32612.
[43] L.Y. Chen, R. Luque, Y.W. Li, Controllable design of tunable nanostructures inside metal–organic frameworks, Chem. Soc. Rev. 46 (2017) 4614–4630.
[44] Y.C. Wei, C.X. Chen, S. Zhai, M. Tan, J.B. Zhao, X.W. Zhu, L. Wang, Q. Liu, T. Dai, Enrofloxacin/florfenicol loaded cyclodextrin metal-organic-framework for drug delivery and controlled release, Drug Deliv. 28 (2021) 372–379.
[45] T. Rajkumar, D. Kukkar, K.H. Kim, J.R. Sohn, A. Deep, Cyclodextrin-metal–organic framework (CD-MOF): From synthesis to applications, J. Ind. Eng. Chem. 72 (2019) 50–66.
[46] Y.Z. He, X.F. Hou, Y. Liu, N.P. Feng, Recent progress in the synthesis, structural diversity and emerging applications of cyclodextrin-based metal–organic frameworks, J. Mater. Chem. B 7 (2019) 5602–5619.
[47] W. Huang, G.B. Hu, W.B. Liang, J.M. Wang, M.L. Lu, R. Yuan, D.R. Xiao, Ruthenium(II) complex-grafted hollow hierarchical metal–organic frameworks with superior electrochemiluminescence performance for sensitive assay of thrombin, Anal. Chem. 93 (2021) 6239–6245.
[48] S. Ali Akbar Razavi, A. Morsali, Linker functionalized metal-organic frameworks, Coord. Chem. Rev. 399 (2019), 213023.
[49] A.R. Echarri, P.A.D. Gonçalves, C. Tserkezis, F.J. García de Abajo, N.A. Mortensen, J.D. Cox, Optical response of noble metal nanostructures: quantum surface effects in crystallographic facets, Optica 8 (2021) 710–721.
[50] S.Y. Song, X. Wang, H.J. Zhang, CeO_2-encapsulated noble metal nanocatalysts: enhanced activity and stability for catalytic application, NPG Asia Mater. 7 (2015) e179-e179.
[51] D. Wen, A.K. Herrmann, L. Borchardt, F. Simon, W. Liu, S. Kaskel, A. Eychmüller, Controlling the growth of palladium aerogels with high-performance toward bioelectrocatalytic oxidation of glucose, J. Am. Chem. Soc. 136 (2014) 2727–2730.
[52] L. Yang, Y.Y. Li, Y. Zhang, D.W. Fan, X.H. Pang, Q. Wei, B. Du, 3D Nanostructured palladium-functionalized graphene-aerogel-supported Fe_3O_4 for enhanced $Ru(bpy)_3^{2+}$-based electrochemiluminescent immunosensing of prostate specific antigen, ACS Appl. Mater. Interfaces 9 (2017) 35260–35267.
[53] Q.Q. Huang, Y. Hu, Y. Pei, J.H. Zhang, M.L. Fu, In situ synthesis of TiO_2@NH_2-MIL-125 composites for use in combined adsorption and photocatalytic degradation of formaldehyde, Appl. Catal. B 259 (2019), 118106.
[54] B. Zhang, J.X. Huang, K.X. Liu, Z.X. Zhou, L.M. Jiang, Y.Q. Shen, D. Zhao, Biocompatible cyclodextrin-based metal–organic frameworks for long-term sustained release of fragrances, Ind. Eng. Chem. Res 58 (2019) 19767–19777.

Xiaofei Li is a master student in school of chemistry and chemical engineering, University of Jinan. His current research interests are electrochemiluminescence sensor and nanomaterials.

Xiang Ren received his B.S. degrees in Chemistry of Materials/English from University of Jinan in 2012, M.S. degree in Chemical Engineering and Technology from University of Jinan in 2015, and Ph.D. degree from University of Jinan/University of Electronic Science and Technology of China in 2019. Now, he is an associate professor in University of Jinan. His main research interests are energy catalysis, nanomaterials controlled-synthesis, and electrochemical biosensors.

Lei Yang received his B.S. and Ph.D. in University of Jinan in 2016 and 2022, respectively. His interests are nanomaterials-based electrochemiluminescence biosensors and immunoassay for biomarkers.

Wei Wang received his B.S. degree in analytical chemistry from University of Jinan (China) in 1983. Now he is a senior engineer in analytical chemistry at Logistics Management Center of Yantai Customs District. His research interest is the safety and health inspection and quarantine of imported and exported food and commodities.

Dawei Fan received her Ph. D degree from Lanzhou Institute of Chemical Physics, Chinese Academy of Sciences. She is currently an associate professor at University of Jinan. Her main research interests include electrochemical sensors and photoelectrochemical sensors. She has published over 50 papers.

Xuan Kuang obtained her Ph.D. in Analytical Chemistry in 2015. Her research interests focus on metal organic materials and their application in electrochemical sensors, and fundamental electrochemical studies of energy storage devices and synthetic nanomotors.

Xu Sun received her Ph.D. in inorganic chemistry at University of Science and Technology of China (USTC). She is now working as an associate professor in School of Chemistry and Chemical Engineering in University of Jinan. Currently, her research interests focus on the design and fabrication of novel nanomaterials for the construction of energy-related devices.

Qin Wei, a professor and DSc, has devoted herself to analytical teaching and scientific research. Her main research interests are the determination of protein and nucleic acid by photometry and the electrochemical immunosensor preparation. She has published over one hundred articles on analysis, immunosensor and applied successfully for many research projects, such as Biomaterials, Adv. Funct. Mater., Biosens. Bioelectron., Sens. Actuators B: Chem., Talanta.

Huangxian Ju received his BS, MS and Ph.D. degrees from Nanjing University during 1982–1992. He was a postdoc in Montreal University (Canada) from 1996 to 1997 and a guest professor in three universities of Germany and Ireland in 1999–2000. He became an associate and full professor of Nanjing University in 1993 and 1999. He is currently the director of State Key Laboratory of Analytical Chemistry for Life Science. His research interests focus on analytical biochemistry, biosensing and molecular diagnosis. He has published 13 books and 785 papers in different journals with SCIE h-index of 100 (>37,500 citations) and Google Scholar h-index of 109 (> 43600 citations).